Atomic-Scale Insights into Electronic, Structural, Dielectric, and Ferroelectric Properties of Ba(Zr, Ti)O_3 Perovskites

Bingcheng Luo[1]*, Zhesi Zhang[1], Mengyang Li[1], Huanxin Li[2], Zili Zhang[3], Hongzhou Song[4]

[1] College of Science, China Agricultural University, Beijing 100083, P. R. China

[2] Department of Chemistry, Physical & Theoretical Chemistry Laboratory, University of Oxford, South Parks Road, Oxford OX1 3QZ, United Kingdom

[3] School of Science, China University of Geosciences, Beijing 100083, P. R. China

[4] Institute of Applied Physics and Computational Mathematics, Beijing 100094, P.R. China

Abstract: Ba(Zr, Ti)O_3 perovskites are promising lead-free piezoelectric and relaxor ferroelectric materials for energy storage and harvest devices, of which the ferroelectric mechanism has long been ambiguous. We theoretically investigated the ferroelectric mechanism from the electronic and atomic scale using first-principles calculation based on density functional theory and density functional perturbation theory. With increasing zirconium content, it is obtained a lattice expansion and a decrease in the ferroelectric polarization in agreement with experiment. An unstable zone-center phonon mode is observed in the polar ferroelectric phase, which tends to stabilizein the nonpolar paraelectric phase, which is associated with the engineering of the relative displacement of the B-site ions that alters the short-range force. The newly formed Ti/Zr (d_{zx},d_{yz})-O ($2p_x$,$2p_y$) π-type bonds are discovered to be the origin of the Ba(Zr, Ti)O_3ferroelectric instability and polarization. Local relaxation strains caused by lattice misalignment of the ionic displacements of Ti ions and Zr ions suppress the polarization of Ba(Zr, Ti)O_3 by counteracting the off-centering of Ti ions and adjacent Zr ions in certain directions.

Keywords: ferroelectric polarization; ferroelectric instability; lattice dynamics; phonon dispersion; barium zirconate titanate

1. Introduction

Ferroelectric perovskite materials have been playing important roles in various technological fields, such as capacitors, memories, sensors, actuators, and energy storage and harvesting devices[1-5]. Among these, barium titanate ($BaTiO_3$) has attracted extensive experimental and theoretical study since its discovery of ferroelectric behavior in 1945 and 1946[6]. It undergoes a series of phase transitions from orthorhombic and rhombohedral ferroelectric phases at low temperature into a tetragonal ferroelectric phase with polarization along the [001] and then transforms to a cubic paraelectric phase with no net polarization direction above 120 ℃.

Understanding the origin of these phase transition of $BaTiO_3$ mainly focuses on the *soft-phonon* models, which considers the transition as displacive and induced by the softening of a zone-center TO mode as the transition temperature is approached[7]. Atomistic displacement of Ti^{4+} cations from the [TiO_6] octahedral center to an off-center position causes the ferroelectric polarization[3]. It was understood that the balance of long-range Coulomb interactions *versus* closed-shell ionic interactions, with the balance tipped by smaller effects related to covalency between d-orbital of metallic ions and O 2p-orbital, contributes to the ferroelectricity in perovskites[8]. First-principles calculations provide support for this hybridization between O 2p states and B-site metallic ions d states, and the giant anomalous Born effective charges reveal evidence for the ferroelectric instability yielded by the large destabilizing Coulomb interaction[9, 10].

Dielectric and ferroelectric properties of $BaTiO_3$ can be tuned by introducing doping elements into the cationic sub-lattice, which also broadens their application. For instance, both permittivity and Curie temperature can be tunable in a large range in the $BaTiO_3$–

$SrTiO_3$ solid solution [11]. Oxygen vacancies in $BaTiO_{3-\delta}$ produced itinerant electrons, partially stabilizing the ferroelectric phases in metallic $BaTiO_{3-\delta}$ by screening strong crystal field perturbations[12]. Temperature stability was broadened from -55 ℃ to 300 ℃ for Ce-doped $BaTiO_3$[13], while the stable unipolar resistive switching characteristics was demonstrated in Co-doped $BaTiO_3$[14]. Oxyhydride of $BaTiO_3$ was found to exhibit hydride exchange and electronic conductivity[15]. With isovalent zirconium substituting titanium, $Ba(Zr_xTi_{1-x})O_3$ (BZT) solid solutions exhibit decreasing ferroelectric transition temperature from 405 K to ~350 K for $x = 0.15$[16]. Considered as the promising lead-free piezoelectric and relaxor ferroelectric systems, BZT solid solution have been receiving continuous attention both experimentally[17-21] and theoretically[22, 23]. First-principles supercell calculations on $BaTi_{0.74}Zr_{0.26}O_3$ showed Ti/Zr distribution determined the Ti displacement and underlined the structural mechanisms involved random local strain effects that lead to disordered Ti displacements[24]. The nonlinear permittivity of BZT for $0.25 \leq x \leq 0.35$ was measured and the Zr^{4+} concentration was evidenced to control the crossover from ferroelectric to relaxor behavior in isovalent BZT ceramics[25]. The dynamic behavior of BZT ceramics with Zr concentration ($0.3 \leq x \leq 0.6$) was described by the development of an order parameter via mean field theory[26]. For the case of BZT with $x = 0.5$, the direct and the field-cooled susceptibility and the Edwards-Anderson order parameter were calculated using first-principles based effective Hamiltonian approach[27]. Despite that large progress has been made in the past few years, there is still a lack of deep understanding of the ferroelectric mechanism, which hinders the fine tuning and meticulous engineering of the BZT ceramics. In this work, we report a detailed theoretical

study aimed at revealing the intrinsic mechanisms of the ferroelectric properties of $Ba(Zr_xTi_{1-x})O_3$ with $0 \leq x \leq 0.5$.

2. Computational methods

The polarization behaviors, lattice dynamics, electronic structure, band structure, and orbital hybridization of $Ba(Zr_xTi_{1-x})O_3$ with $0 \leq x \leq 0.5$ (Fig. 1) were computed from first-principles calculations, which are based on density functional theory (DFT) as implemented in Vienna ab initio simulation package (VASP) [28, 29]. Kohn-Sham energy with respect to the basis set and the sampling of reciprocal space were employed to minimize the variation in the lattice vibrations. The exchange and correlation effects are treated within the generalized gradient approximation (GGA) with a Perdew–Burke–Ernzerhof revised for solids (PBEsol) exchange-correlation functional[30]. The scalar-relativistic projector augmented wave method (PAW) pseudopotentials used for BZT models were constructed by the electron configurations as Ba $5s^25p^66s^2$ states, Ti $3s^23p^63d^24s^2$ states, Zr $4s^24p^65s^24d^2$ and O $2s^22p^4$ states[31]. An energy cut-off of 600 eV was chosen for the number of plane wave bases. Monkhorst-Pack mesh grid with 8×8×8, 8×8×2, 8×8×8, 8×4×2, and 8×8×2 special k-point mesh for BZT models with x = 0, 0.083, 0.125, 0.167, 0.25, and 0.5, respectively, were carried out for the special points sampling integration over the Brillouin zone. [32] The energy tolerance was 1×10^{-8} eV/atom, while the force tolerance was set to 0.001 eV/Å.

Hybrid functional HSE06 is employed to obtain accurate band structures. Born effective charges, phonon frequencies and dielectric properties are calculated using density functional perturbation theory (DFPT) [33, 34] implanted in VASP code and post-processed with the PHONOPY code[35]. The force constants and the dynamical matrix

were obtained from the Hellmann–Feynman forces calculated with small individual displacements of non-equivalent atoms. Both density functional perturbation theory (DFPT) approaches [36] and the finite displacement supercell approaches[37] were tested to construct and evaluate force constants, which produced similar results within the variance in the mode energies of 5 cm^{-1}. The macroscopic electronic polarization is calculated by using the Berry phase method[38]. The fitted energy-polarization curve and temperature-dependence relationship were performed using a homemade program, which is developed based on electrostatics displacement field and Landau-Ginsburg-Devonshire (LGD) theory.

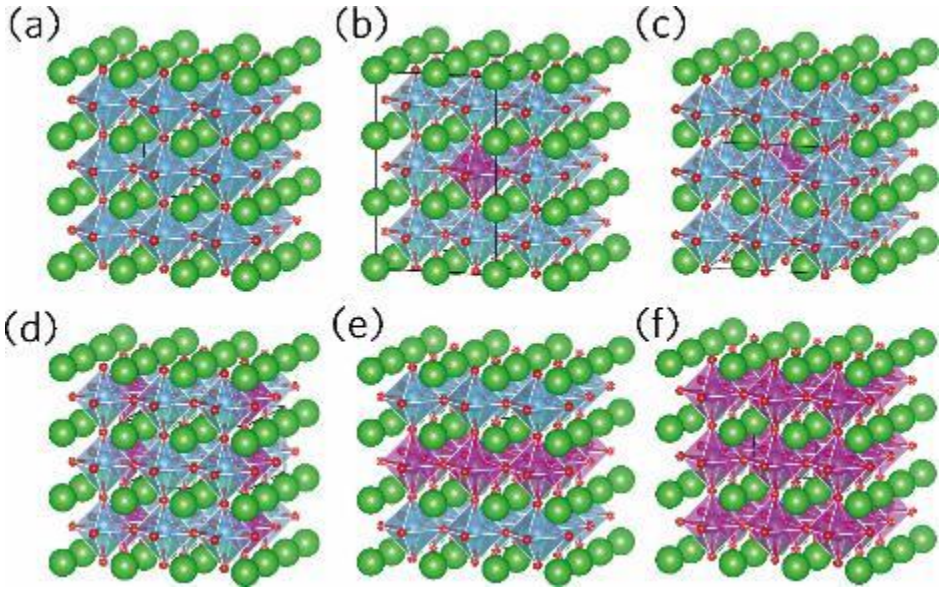

Fig. 1. Lattice models of Ba(Zr, Ti)O_3. (a) x = 0, (b) x = 0.083, (c) x = 0.125, (d) x = 0.25, (e) x = 0.5. (f) x = 1.0. The Ti cation represented by a cyan sphere is at the center of the unit cell and is six-fold coordinated to oxygen represented by a red sphere. Ba cation is represented by a green sphere. Zr cation is represented by a red sphere.

3. Results and discussion

BZT superlattices were constructed based on tetragonal $BaTiO_3$ lattice with Zr-substitution of Ti. Fig. 1 shows the $Ba(Zr, Ti)O_3$ structure with various contents of Zr. For the pure tetragonal $BaTiO_3$, the calculated lattice constant a = b = 3.98 Å, and c = 4.03 Å, which is in great consistence with experimental results[39]. The calculated equilibrium lattice constants of $Ba(Zr_xTi_{1-x})O_3$ with $0 \leq x \leq 0.5$ are listed in Table 1. The lattice parameters of $Ba(Zr_xTi_{1-x})O_3$ were found to increase with substitution content, which is also experimentally observed in the polycrystalline samples of Zr-doped $BaTiO_3$ prepared by conventional solid state reaction method [40].

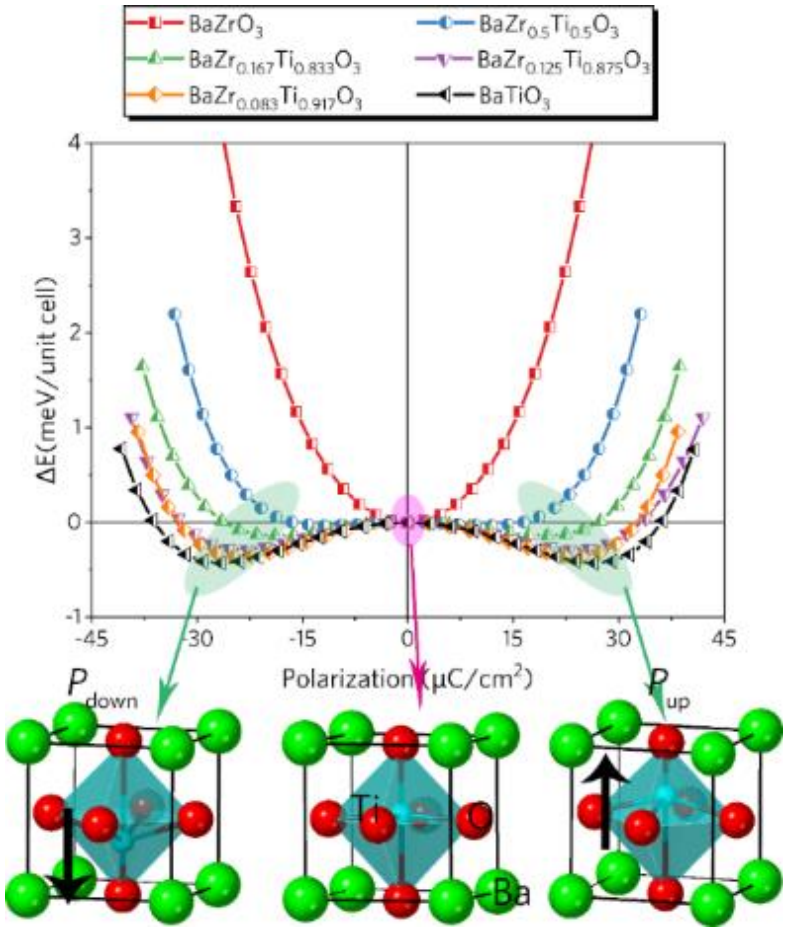

Fig. 2. Total energy change due to bulk ferroelectric soft-mode distortion is calculated as a function of ferroelectric polarization for different chemical composition of Ba(Zr, Ti)O_3. Bottom panels show the atomic configuration of $BaTiO_3$ with the polarization switching.

Table 1 Computational parameters of $Ba(Zr_xTi_{1-x})O_3$ with $0 \leq x \leq 0.5$ after geometry relaxation, including the converged energy and force threshold, the plane-wave cutoff and k-point mesh.

x	a (Å)	b (Å)	c (Å)	*V* (Å^3)	Cutoff (eV)	k points	Energy (eV/atom)	Forces (eV/ Å)
0.0	3.98	3.98	4.03	64.13	600	8×8×8	10^{-8}	10^{-3}
0.083	8.03	8.03	12.69	818.97	600	8×8×2	10^{-8}	10^{-3}
0.125	8.01	8.01	8.15	522.52	600	8×8×8	10^{-8}	10^{-3}
0.167	4.11	8.19	12.28	413.25	600	8×4×2	10^{-8}	10^{-3}
0.25	8.04	8.04	4.15	268.03	600	8×8×2	10^{-8}	10^{-3}
0.5	4.19	4.19	8.33	146.07	600	8×8×2	10^{-8}	10^{-3}

1.0	4.19	4.19	4.19	73.77	600	8×8×8	10^{-8}	10^{-3}

Variation of total energy affected by the bulk ferroelectric soft-mode distortion as a function of ferroelectric polarization for different chemical composition of Ba(Zr, Ti)O_3. is obtained, as shown in Fig. 2. Bottom panels show the atomic configuration of $BaTiO_3$ with the polarization switching. The Ti cation represented by a cyan sphere is at the center of the unit cell and is six-fold coordinated to oxygen represented by a red sphere. Ba cation is represented by a green sphere. The total energy of paraelectric phase is taken as a reference. The double minima show the down and up polarization variations. For the paraelectric phase of $BaTiO_3$ with cubic structure, B-site cations are in the center of crystal lattice and symmetric to the neighboring ions. The ferroelectric soft-mode distortion is characterized by the shift of the B-site cation such as Zr and Ti cations with respect to the surrounding O-ion octahedron. A net macroscopic electrical polarization is produced through breaking inversion symmetry by the internal distortion. The total energy of paraelectric phase is taken as a reference, while the minima of double-curve represents the ferroelectric phase. As seen from Fig. 2, ferroelectric $BaTiO_3$ and Ba(Zr, Ti)O_3 exhibit a deep double-well profile with two global energy minimum as the off-center position, similar to what is shown by other reports about ferroelectric materials such as $LaFeO_3$[41], thin layer of ferroelectric $Hf_{0.5}Zr_{0.5}O_2$ [42], multiferroic $BiFeO_3$ [43] and others. On the other hand, $BaZrO_3$ exhibits a single well profile with only one energy minimum at the central position. The calculated polarization for the ferroelectric tetragonal $BaTiO_3$ is 29.1 $\mu C/cm^2$ which is in good agreement with other results[9, 44]. With the increase of Zr cation amount, the spontaneous polarization of Ba(Zr, Ti)O_3 displays a decreasing trend, which is observed in the experimental ceramics[17, 45]. For the case of x = 0.083, the ferroelectric polarization of Ba(Zr, Ti)O_3 is 27.2 $\mu C/cm^2$. The ferroelectric polarization of Ba(Zr, Ti)O_3

is 26.5 μC/cm^2 for x = 0.167, 21.1 μC/cm^2 for x = 0.25, and 23.0 μC/cm^2 for x = 0.5, respectively. At the same time, the well-depth of energy-polarization profile exhibits reduction as the increase of Zr amount. The reduction in well-depth and spontaneous polarization is attributed to the larger ionic offset and stronger hybridization of Zr 4d to O 2p and Ba 3d to O 2p states.

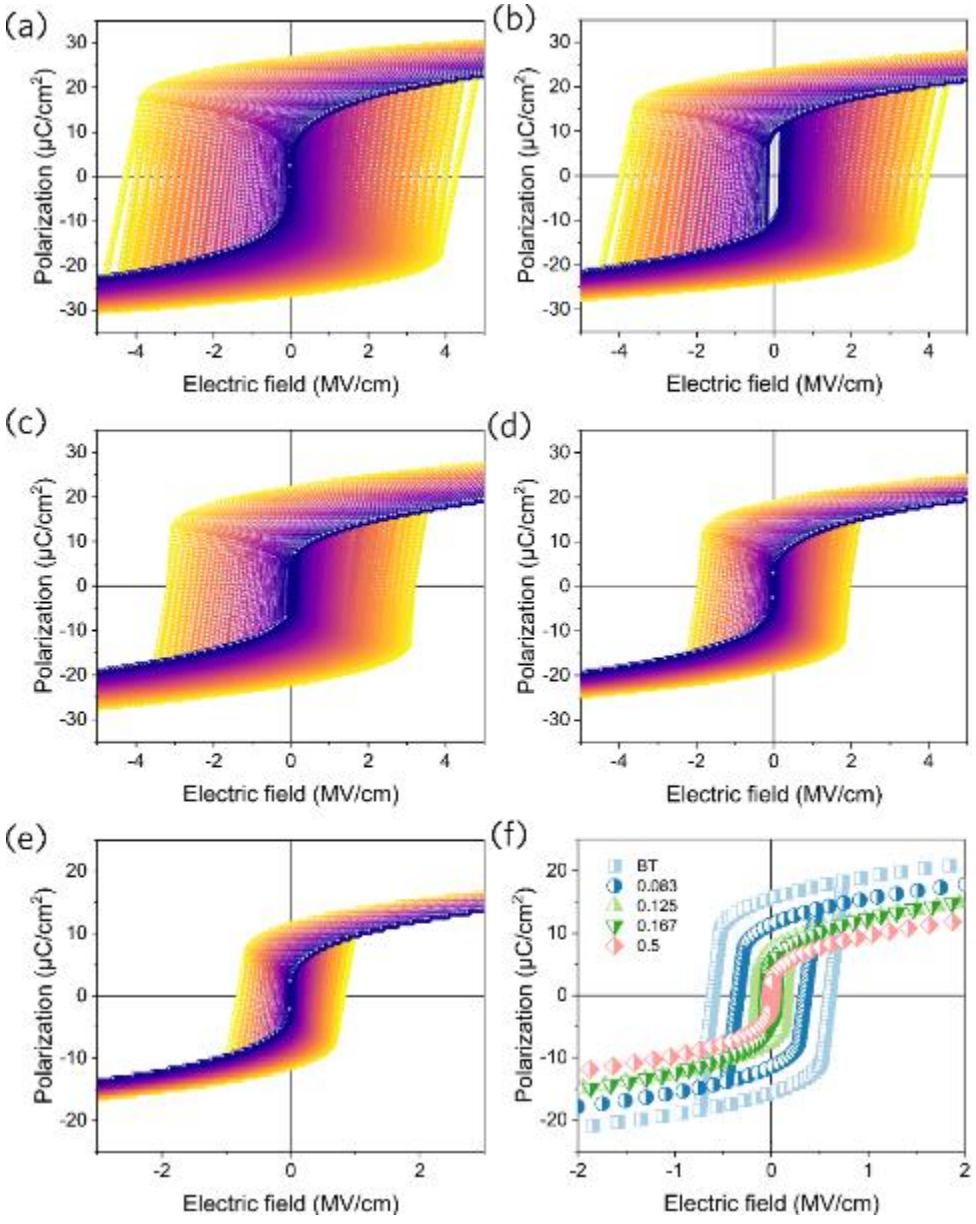

Fig. 3. Temperature dependence of the ferroelectric hysteresis of $Ba(Zr_xTi_{1-x})O_3$ with various composition. (a) $x = 0$, (b) $x = 0.083$, (c) $x = 0.125$, (d) $x = 0.167$, (e) $x = 0.5$. (f) Composition dependence of the ferroelectric hysteresis of $Ba(Zr_xTi_{1-x})O_3$ at 295 K.

The temperature dependence of ferroelectric hysteresis is calculated from phenomenological Landau-Ginsburg-Devonshire (LGD) theory, as shown in Fig. 3. Ferroelectric loops of $Ba(Zr_xTi_{1-x})O_3$ are found to shrink with the increase of temperature, which result from the phase transition of the ferroelectric tetragonal phase to the paraelectric cubic phase. At temperatures far below phase transition temperature, near-square ferroelectric P-E loops with high remnant polarization are observed. As the temperature increases, remnant polarization decreases and the coercive field decreases simultaneously, which is in good consistence with the experimental results of $Ba(Zr_xTi_{1-x})O_3$ ceramics [46-48]. In Fig. 3(f), with the increased amount of zirconium ions, the remnant polarization, maximum polarization and nonlinearity are reduced, which is observed in the manganese-doped $Ba(Zr_xTi_{1-x})O_3$ ceramics [49].

Phonon dispersion curves of various BZT models are achieved. Fig. 4(a) shows the phonon dispersion for tetragonal $BaTiO_3$ with the structure at the minimum state of double well landscape. The transverse optic modes are unstable at the Γ point and become stable along Γ-M and Γ-R directions resulted from the volume elongation along [001] directions, which is in good agreement with other computational and experimental results[50-52]. Analysis of phonon dispersion for Ba(Zr, Ti)O_3 with various composition shown in Fig. 4(b,c) reveals the disappearance of imaginary frequencies at the Γ point, indicating that the ground state of paraelectric Ba(Zr,Ti)O_3 is nonpolar tetragonal phase. In contrast, the ferroelectric Ba(Zr,Ti)O_3 shows highly unstable phonon modes. The strongest instabilities are observed at the Γ point with an irreducible representation Γ15. For the case of

$Ba(Zr_xTi_{1-x})O_3$ with x = 0.083 and 0.125, all phonon modes at the high K-point boundaries are unstable with a maximum imaginary frequency of 5.59i THz, and 5.20i THz, respectively. For the case of pure $BaZrO_3$ containing no Ti ions, all the transverse optic modes are stable at the high symmetry point. For the case of $Ba(Zr_xTi_{1-x})O_3$ with x = 0.25 and 0.5, phonon branches along G-X and G-Z-R are unstable while the phonon mode at M point is stable. The maximum imaginary frequencies are 4.96i THz and 8.83i THz. The imaginary modes are derived from the relative translation of B-site ions relative to O ions. This suggests that the solidification of the Γ15 unstable mode in the tetragonal ferroelectric phase would directly drive the system to the nonpolar state. We thus performed a full relaxation of the cell. Indeed, we obtained the nonpolar state phase as shown in Fig. 4(g,h,i). Experimentally, paraelectric phase of $BaTiO_3$ and Ba(Zr, Ti)O_3 are nonpolar state, while the ferroelectric phases are polar states with the characteristic of ferroelectric hysteresis. Herein the direct proof is provided for the transition between polar state to nonpolar states as evidenced from the phonon dispersion curve, which contradicts previous reports that state the existence of unstable phonon mode in nonpolar paraelectric phase.

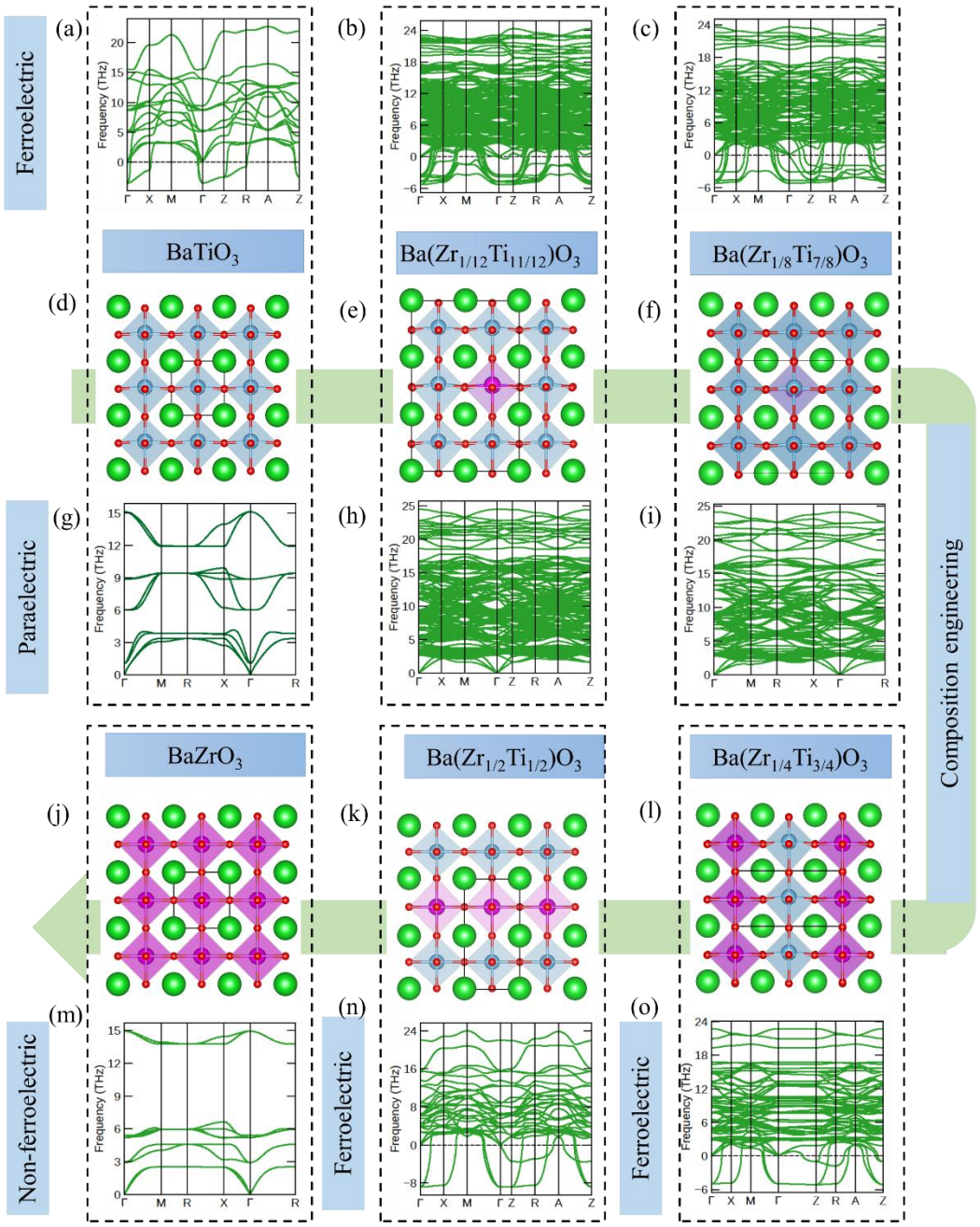

Fig. 4. Phonon dispersion curves of paraelectric and ferroelectric phase of Ba(Zr, Ti)O_3 under different composition, together with the corresponding lattice structures. Imaginary frequencies are plotted as negative values. Paraelectric phase shows all stable phonon modes, while ferroelectric phase shows unstable imaginary phonon branches.

Electronic band structure along the high symmetry directions in the first Brillouin zone is presented in Fig. 5. Hybrid exchange functional HSE06 is employed, which can give more accurate band gaps than the conventional GGA or LDA functional. The band gap of $BaTiO_3$ derived from the HSE06 calculations is 3.00 eV, which is in good agreement with the experimental and other theoretical values [53, 54]. As the zirconium content increases, the band structure become more complex with increased band levels. The valence band near the Fermi surface of BZT are in energy from -5 to 0 eV and the conduction band is in the energy from 2 to 10 eV, enabling the whole system to exhibit semiconductor properties. HSE06 bandgaps for $Ba(Zr_xTi_{1-x})O_3$ where x = 0.083, 0.125, 0.167, and 0.25 are 3.17 eV, 3.20 eV, 3.05 eV, 3.04 eV and 3.6 eV, respectively. The increased bandgap provides support for the experimental improvement in insulation ability and decline in dielectric loss.

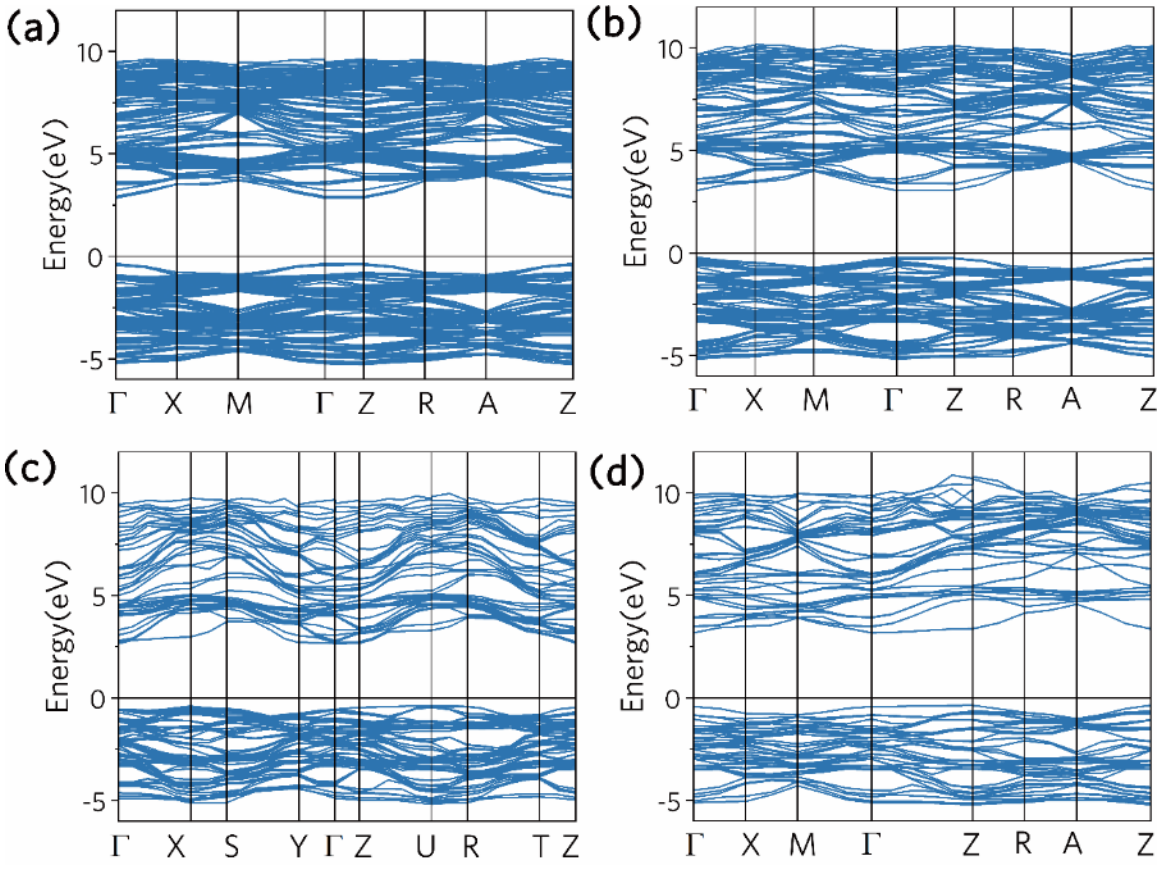

Fig. 5. Band structure of $Ba(Zr_xTi_{1-x})O_3$ from HSE06 calculations with various composition. (a) x = 0.083, (b) x = 0.125, (c) x = 0.167, (d) x = 0.25.

To further analyze the origin of ferroelectric properties, the total and partial density of states of $Ba(Zr_xTi_{1-x})O_3$ are studied as shown in Fig. 6 and Fig. 8. The symmetric spin up and spin down states reveals no magnetism. From the energy band level in Fig. 6(b), the lower valence band located at -60eV, -50eV and -36eV is mainly occupied by the Ti 4s, Zr 5s and Ti 3p orbitals. Zr 4p and Ba 6s orbitals contribute to the energy band at -27eV, O 2s orbital contributes to the energy band at -18eV, and Ba 5p orbital contributes to the energy band at -11eV. The valence band in the energy range of -5 eV to 0 eV is mainly attributed by the O 2p states, with some mixing of Ti 3d and Zr 4d states shown in Fig.

8(a-b). The conduction band in the energy range of 2 eV to 10 eV is mainly attributed to the Ti 3d states, with some mixing of O 2p and Zr 4d states as shown in Fig. 8(a-b). This hybridization of Ti 3d, O 2p, and Zr 4d is a characteristic for ferroelectric $Ba(Zr_xTi_{1-x})O_3$.

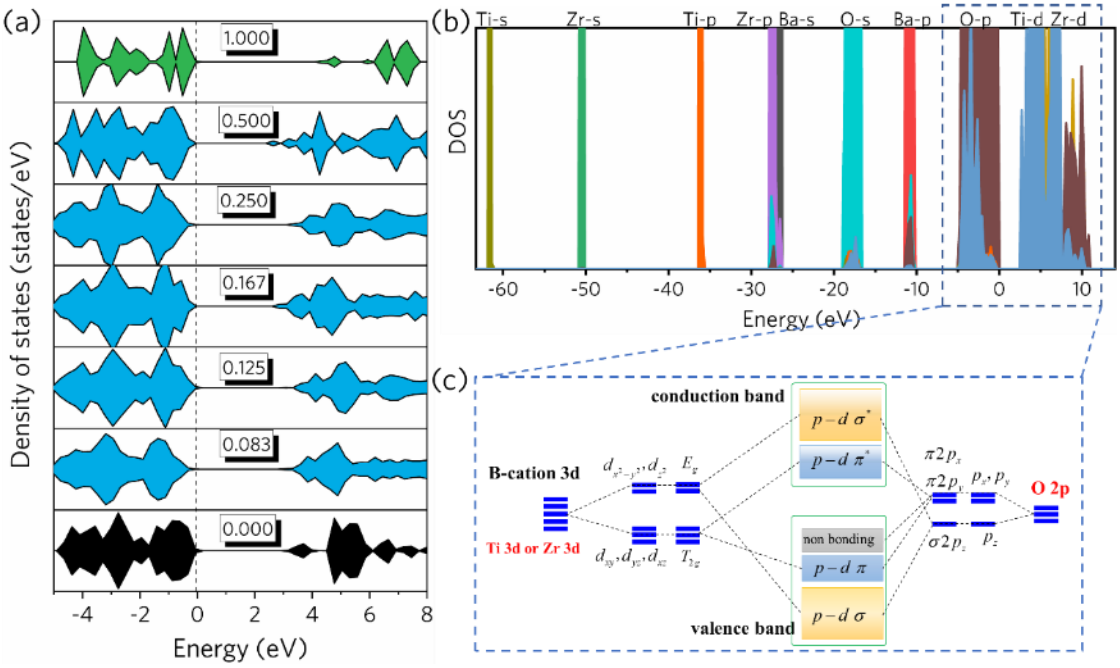

Fig. 6.(a) Compositional dependence of total density of states of $Ba(Zr_xTi_{1-x})O_3$, revealing no magnetism from the symmetric spin up and spin down states. (b) Energy band level and (c) molecular orbital diagram of $Ba(Zr_xTi_{1-x})O_3$.

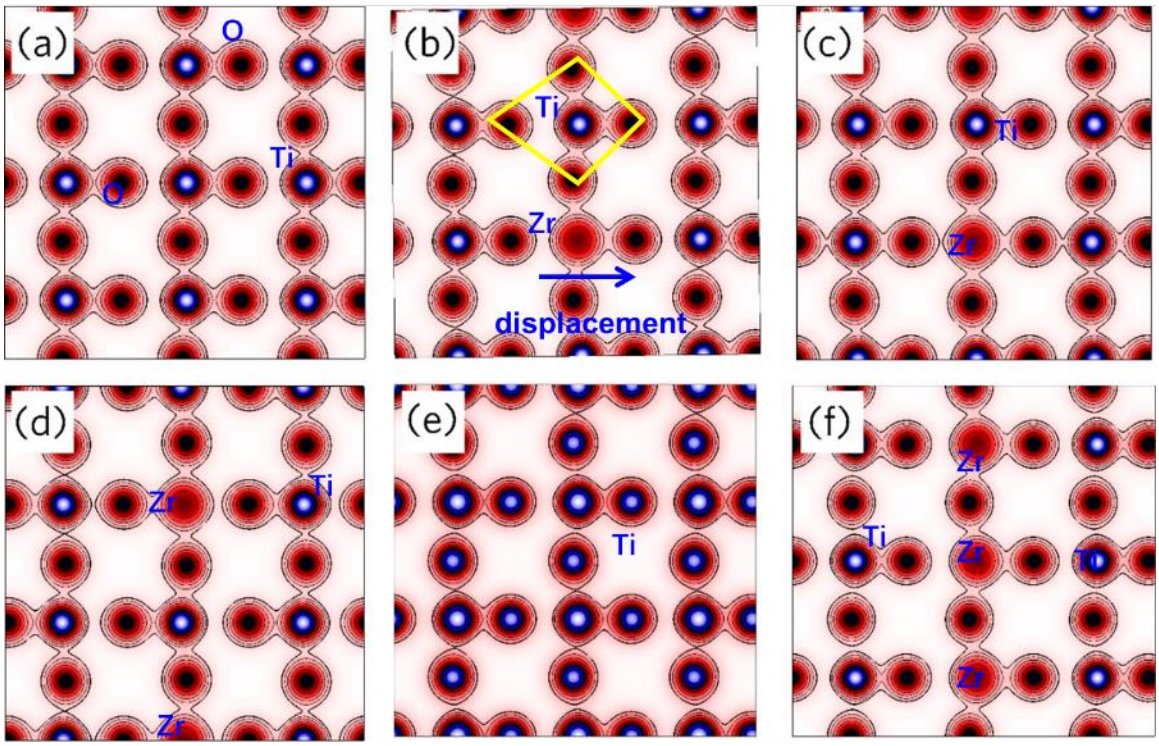

Fig. 7. Charge density mapping of $Ba(Zr_xTi_{1-x})O_3$ with various composition. (a) x = 0, (b) x = 0.083, (c) x = 0.125, (d) x = 0.167, (e) x = 0.25, (f) x = 1.

To obtain deeper analysis of the orbital hybridization, charge density mapping, molecular orbitals and lm-decomposed density of states of $Ba(Zr_xTi_{1-x})O_3$ are investigated, as shown in Fig. 6(c), Fig. 7, and Fig. 8(c), respectively. Five d-orbitals of B-site Ti or Zr split into two types, namely, triply degenerated $T_{2g}(d_{xy},d_{yz},d_{zx})$ in the lower energy level and doubly degenerated E_g (d_{x2-y2},d_{z2}) in the higher energy level. The hybridization of Eg (d_{x2-y2},d_{z2}) with O 2pz orbitals form the p-d σ-type bond at valence bond and p-d σ-type anti-bond at conduction bond, which further construct the three-dimensional framework of oxygen octahedron. The hybridization of $T_{2g}(d_{xy},d_{yz},d_{zx})$ with O 2p (px, py) form the p-d π-type bond at valence bond and p-d π-type anti-bond at conduction bond. The introduction of Zr ions induced the off-center B-site displacement (Fig. 7), which split T_{2g} orbitals into d_{xy} and (d_{yz},d_{zx}) orbitals. Therefore, strong hybridization of Ti $3d_{zx}$-$O2p_x$ π-type bond, Zr $4d_{zx}$-

$O2p_x$ π-type bond, Ti $3d_{yz}$-$O2p_y$ π-type bond, and Ti $3d_{yz}$-$O2p_y$ π-type bond is produced. This π-type bond is the origin of ferroelectric properties and the dynamic instability of $Ba(Zr_xTi_{1-x})O_3$. It was found that the substitution of Zr for Ti strongly favors short-range repulsive forces, while the larger size of Zr ions locally favors long-range interactions along the O-Ti-O-Ti-O chain[55]. Local relaxation strains caused by lattice misalignment of the ionic displacements of Ti and Zr ions therefore suppress the polarization of $Ba(Zr_xTi_{1-x})O_3$ compared with $BaTiO_3$ by cancelling out the off-centering of Ti ions and adjacent Zr ions in certain directions.

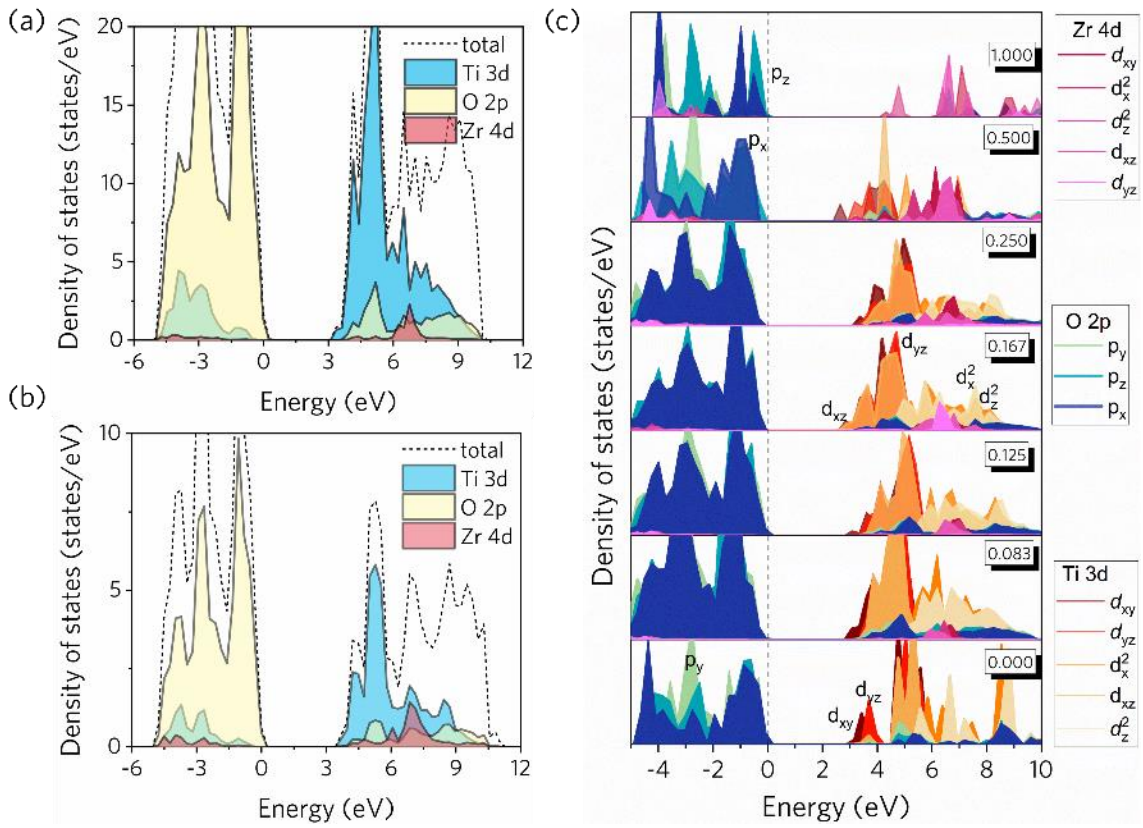

Fig. 8. Density of states of $Ba(Zr_xTi_{1-x})O_3$ from HSE06 calculations with various composition. (a) x = 0.083, (b) x = 0.25, (c) Compositional dependence *lm*-decompsoed density of states of O2p, Ti 3d, and Zr 4d orbitals.

4. Conclusions

In this work, we investigated the polarization behaviors, lattice dynamics, electronic structure, band structure, and orbital hybridization of Ba(Zr, Ti)O_3 and analyzed the origin of the ferroelectric mechanism from the electronic and atomic point of view using first-principles calculations. Substitution of Zr with Ti ions raises the lattice parameters and reduces the ferroelectric polarization, which was also observed in the experimental ceramics and confirmed high validity of the as-performed calculations. The increasing bandgap with increasing zirconium content provides support for the experimental improvement in insulation ability and reduction in dielectric loss. An unstable zone-center phonon mode is observed for the polar ferroelectric phase, which becomes stabilized in the nonpolar paraelectric phase associated with the modification of the short-range forces by engineering the relative displacements of B-site ions. The newly formed Ti/Zr (d_{zx},d_{yz})-O ($2p_x$,$2p_y$) π-type bond is discovered to be the origin of the ferroelectric instability and the ferroelectric polarization of Ba(Zr, Ti)O_3. Local relaxation strains caused by lattice misalignment of the ionic displacements of Ti and Zr ions suppress the polarization of Ba(Zr, Ti)O_3 compared with $BaTiO_3$ by cancelling out the off-centering of Ti ions and adjacent Zr ions in certain directions.

Declaration of competing interest

The authors declare that they have no known competing financial interests or personal relationships that could have appeared to influence the work reported in this paper.

Acknowledgements

This research was supported by High-performance Computing Platform of China Agricultural University and the National Natural Science Foundation of China (Grant No. 52202154). The work was carried out at National Supercomputer Center in Tianjin, and the calculations were performed on Tianhe new generation supercomputer.

Data Availability Statement:

The data that support the findings of this study are available from the corresponding author upon reasonable request.

References

[1] M. Li, M.J. Pietrowski, R.A. De Souza, H. Zhang, I.M. Reaney, S.N. Cook, J.A. Kilner, D.C. Sinclair, Nature Materials, 13 (2014) 31-35.
[2] K.J. Choi, M. Biegalski, Y.L. Li, A. Sharan, J. Schubert, R. Uecker, P. Reiche, Y.B. Chen, X.Q. Pan, V. Gopalan, L.Q. Chen, D.G. Schlom, C.B. Eom, Science, 306 (2004) 1005-1009.
[3] R.E. Cohen, Nature, 358 (1992) 136-138.
[4] B. Luo, X. Wang, E. Tian, H. Song, H. Wang, L. Li, ACS Appl Mater Interfaces, 9 (2017) 19963-19972.
[5] B. Luo, X. Wang, E. Tian, H. Song, Q. Zhao, Z. Cai, W. Feng, L. Li, J. Eur. Ceram. Soc. (Netherlands), 38 (2018) 1562-1568.
[6] W. B., Nature, 157 (1946) 808-808.
[7] R. Yu, H. Krakauer, Physical Review Letters, 74 (1995) 4067-4070.
[8] S.V. Halilov, M. Fornari, D.J. Singh, Physical Review B, 69 (2004) 174107.
[9] Y. Wang, X. Liu, J.D. Burton, S.S. Jaswal, E.Y. Tsymbal, Physical Review Letters, 109 (2012) 247601.
[10] P. Ghosez, X. Gonze, J.P. Michenaud, Europhysics Letters (EPL), 33 (1996) 713-718.
[11] B. Luo, X. Wang, E. Tian, H. Qu, Q. Zhao, Z. Cai, H. Wang, W. Feng, B. Li, L. Li, Journal of the American Ceramic Society, 101 (2018) 2976-2986.
[12] T. Kolodiazhnyi, M. Tachibana, H. Kawaji, J. Hwang, E. Takayama-Muromachi, Phys Rev Lett, 104 (2010) 147602.
[13] M. Wang, L. Li, N. Zhang, Y. Liu, J. Chen, Journal of the American Ceramic Society, 96 (2013) 3046-3049.
[14] Z. Yan, Y. Guo, G. Zhang, J.-M. Liu, Advanced Materials, 23 (2011) 1351-1355.

[15] Y. Kobayashi, O.J. Hernandez, T. Sakaguchi, T. Yajima, T. Roisnel, Y. Tsujimoto, M. Morita, Y. Noda, Y. Mogami, A. Kitada, M. Ohkura, S. Hosokawa, Z. Li, K. Hayashi, Y. Kusano, J.e. Kim, N. Tsuji, A. Fujiwara, Y. Matsushita, K. Yoshimura, K. Takegoshi, M. Inoue, M. Takano, H. Kageyama, Nature Materials, 11 (2012) 507-511.
[16] D. Nuzhnyy, J. Petzelt, M. Savinov, T. Ostapchuk, V. Bovtun, M. Kempa, J. Hlinka, V. Buscaglia, M.T. Buscaglia, P. Nanni, Physical Review B, 86 (2012) 014106.
[17] Q. Xu, D. Zhan, H.-X. Liu, W. Chen, D.-P. Huang, F. Zhang, Acta Materialia, 61 (2013) 4481-4489.
[18] I.K. Jeong, C.Y. Park, J.S. Ahn, S. Park, D.J. Kim, Physical Review B, 81 (2010) 214119.
[19] C. Filipič, Z. Kutnjak, R. Pirc, G. Canu, J. Petzelt, Physical Review B, 93 (2016) 224105.
[20] C. Laulhé, F. Hippert, J. Kreisel, M. Maglione, A. Simon, J.L. Hazemann, V. Nassif, Physical Review B, 74 (2006) 014106.
[21] D. Wang, A.A. Bokov, Z.-G. Ye, J. Hlinka, L. Bellaiche, Nature Communications, 7 (2016) 11014.
[22] G. Geneste, L. Bellaiche, J.-M. Kiat, Physical Review Letters, 116 (2016) 247601.
[23] R. Pirc, Z. Kutnjak, Physical Review B, 89 (2014) 184110.
[24] C. Laulhé, A. Pasturel, F. Hippert, J. Kreisel, Physical Review B, 82 (2010) 132102.
[25] W. Kleemann, S. Miga, J. Dec, J. Zhai, Applied Physics Letters, 102 (2013).
[26] M. Usman, A. Mumtaz, S. Raoof, S.K. Hasanain, Applied Physics Letters, 103 (2013).
[27] A.R. Akbarzadeh, S. Prosandeev, E.J. Walter, A. Al-Barakaty, L. Bellaiche, Phys Rev Lett, 108 (2012) 257601.
[28] G. Kresse, J. Furthmuller, Phys Rev B Condens Matter, 54 (1996) 11169-11186.
[29] G. Kresse, D. Joubert, Physical Review B, 59 (1999) 1758-1775.
[30] J.P. Perdew, A. Ruzsinszky, G.I. Csonka, O.A. Vydrov, G.E. Scuseria, L.A. Constantin, X. Zhou, K. Burke, Phys Rev Lett, 100 (2008) 136406.
[31] P.E. Blöchl, Phys. Rev. B, 50 (1994) 17953-17979.
[32] H.J. Monkhorst, J.D. Pack, Physical Review B, 13 (1976) 5188-5192.
[33] X. Gonze, Phys. Rev. A, 52 (1995) 1096-1114.
[34] X. Gonze, Physical Review A, 52 (1995) 1086-1095.
[35] A. Togo, I. Tanaka, Scripta Materialia, 108 (2015) 1-5.
[36] S. Baroni, S. de Gironcoli, A. Dal Corso, P. Giannozzi, Reviews of Modern Physics, 73 (2001) 515-562.
[37] R.P. Stoffel, C. Wessel, M.-W. Lumey, R. Dronskowski, Angewandte Chemie International Edition, 49 (2010) 5242-5266.
[38] R.D. King-Smith, D. Vanderbilt, Physical Review B, 47 (1993) 1651-1654.
[39] G. Shirane, H. Danner, R. Pepinsky, Physical Review, 105 (1957) 856-860.
[40] S. Mahajan, O.P. Thakur, C. Prakash, K. Sreenivas, Bulletin of Materials Science, 34 (2011) 1483-1489.
[41] L. Weston, X.Y. Cui, S.P. Ringer, C. Stampfl, Physical Review B, 93 (2016) 165210.
[42] M. Hoffmann, F.P.G. Fengler, M. Herzig, T. Mittmann, B. Max, U. Schroeder, R. Negrea, P. Lucian, S. Slesazeck, T. Mikolajick, Nature, 565 (2019) 464-467.
[43] Y.-L. Huang, D. Nikonov, C. Addiego, R.V. Chopdekar, B. Prasad, L. Zhang, J. Chatterjee, H.-J. Liu, A. Farhan, Y.-H. Chu, M. Yang, M. Ramesh, Z.Q. Qiu, B.D. Huey,

C.-C. Lin, T. Gosavi, J. Íñiguez, J. Bokor, X. Pan, I. Young, L.W. Martin, R. Ramesh, Nature Communications, 11 (2020) 2836.
[44] R. Imura, Y. Kitanaka, T. Oguchi, Y. Noguchi, M. Miyayama, Journal of Advanced Dielectrics, 04 (2014) 1450003.
[45] L. Zhao, X. Ke, W. Wang, M. Fang, A. Xiao, L. He, L. Zhang, J. Gao, Y. Wang, X. Ren, Journal of Alloys and Compounds, 788 (2019) 748-755.
[46] Z. Yu, C. Ang, R. Guo, A.S. Bhalla, Journal of Applied Physics, 92 (2002) 2655-2657.
[47] M. Aghayan, A. Khorsand Zak, M. Behdani, A. Manaf Hashim, Ceramics International, 40 (2014) 16141-16146.
[48] N. Nanakorn, P. Jalupoom, N. Vaneesorn, A. Thanaboonsombut, Ceramics International, 34 (2008) 779-782.
[49] U. Weber, G. Greuel, U. Boettger, S. Weber, D. Hennings, R. Waser, Journal of the American Ceramic Society, 84 (2001) 759-766.
[50] P. Ghosez, E. Cockayne, U.V. Waghmare, K.M. Rabe, Physical Review B, 60 (1999) 836-843.
[51] S. Tinte, M.G. Stachiotti, M. Sepliarsky, R.L. Migoni, C.O. Rodriguez, Journal of Physics: Condensed Matter, 11 (1999) 9679-9690.
[52] Y. Zhang, J. Sun, J.P. Perdew, X. Wu, Physical Review B, 96 (2017) 035143.
[53] S. Mukherjee, D. Phuyal, C.U. Segre, S. Das, O. Karis, T. Edvinsson, H. Rensmo, The Journal of Physical Chemistry C, 125 (2021) 14910-14923.
[54] S. Ramakanth, K.C. James Raju, Journal of Applied Physics, 115 (2014).
[55] C. Mentzer, S. Lisenkov, Z.G. Fthenakis, I. Ponomareva, Physical Review B, 99 (2019) 064111.